A stability analysis of divergence damping on a latitude-longitude grid

JARED WHITEHEAD *

Department of Mathematics, University of Michigan, Ann Arbor, Michigan

CHRISTIANE JABLONOWSKI, RICHARD B. ROOD

Department of Atmospheric, Oceanic and Space Sciences, University of Michigan, Ann Arbor, Michigan

PETER H. LAURITZEN

Climate and Global Dynamics Division, National Center for Atmospheric Research,† Boulder, Colorado

Monthly Weather Review manuscript

revised on March/24/2011

_____

Corresponding author address: Jared Whitehead, 2074 East Hall, 530 Church St., Ann Arbor, MI 48109.

E-mail: jaredwh@umich.edu

†The National Center for Atmospheric Research is sponsored by the National Science Foundation.

ABSTRACT

The dynamical core of an atmospheric general circulation model is engineered to satisfy a delicate balance between numerical stability, computational cost, and an accurate representation of the equations of motion. It generally contains either explicitly added or inherent numerical diffusion mechanisms to control the build-up of energy or enstrophy at the smallest scales. The diffusion fosters computational stability and is sometimes also viewed as a substitute for unresolved subgrid-scale processes. A particular form of explicitly added diffusion is horizontal divergence damping.

In this paper a von Neumann stability analysis of horizontal divergence damping on a latitude-longitude grid is performed. Stability restrictions are derived for the damping coefficients of both second and fourth-order divergence damping. The accuracy of the theoretical analysis is verified through the use of idealized dynamical core test cases that include the simulation of gravity waves and a baroclinic wave. The tests are applied to the finite-volume dynamical core of NCAR's Community Atmosphere Model (CAM) version 5. Investigation of the amplification factor for the divergence damping mechanisms explains how small-scale meridional waves found in a baroclinic wave test case are not eliminated by the damping.

1. Introduction

This paper focuses on the characteristics of an explicit diffusion mechanism in the finite-volume (FV) dynamical core (Lin 2004) that is part of the Community Atmosphere Model CAM version 5 (CAM 5) at the National Center for Atmospheric Research (NCAR) (Neale et al. 2010). A dynamical core is, broadly speaking, that part of an atmospheric General Circulation Model (GCM) associated with the fluid dynamics. It includes both the resolved and subgrid-scale flow. The spatial scale of the resolved flow is determined by the grid spacing of the discrete mesh. The actual "believable scales" of a model are highly dependent on the numerical scheme (Lander and Hoskins 1997). For example, Skamarock (2004) estimated with the help of kinetic energy spectra that the "effective resolution" of the Weather Research and Forecasting (WRF) model is $7\Delta x$ where Δx symbolizes the grid spacing. In any case, subgrid scales smaller than $2\Delta x$ fall below the resolution of the grid. Slightly larger scales (for WRF these are the scales between $2\Delta x$ and $7\Delta x$) are represented by the model, but not resolved effectively. This paper seeks to quantify the effects of diffusive processes on these un- and under-resolved subgrid scales in GCMs. Of particular interest here is the impact of a specific, explicitly added diffusive mechanism on the underresolved scales.

The dynamical core of each model is engineered to satisfy a delicate balance between numerical stability, an accurate representation of the equations of motion, and computational cost. In an effort to balance these factors, each model employs some form of diffusion, filtering or a-posteriori fixers (Williamson et al. 2009). Often these practices are poorly documented, with the presumption that their impact on model performance is small. This presumption is often justified when considering their effect on a fully resolved, isolated wave.

However, model performance is determined by a complex spectrum of motions on many scales and the interactions of these scales. The decay of waves, ultimately, has important implications for the mean circulation of the atmosphere (Andrews and McIntyre 1978). Therefore, relegating this ultimate decay to a set of poorly understood subgrid-scale processes leaves an undocumented impact on the model circulation and possibly the climate statistics in long time integrations. Scientific rigor requires the evaluation of the effects of adding diffusion, filters and fixers (Jablonowski and Williamson 2011). We assert that this might be a particularly important aspect of dynamical cores as we push models to higher resolution in pursuit of more realistic representations of both climate and weather. This assertion is based on the fact that it has been implicit in both model construction and dynamical meteorology that the scales of interest are quasi-nondivergent. This will not be true for models with grid sizes of order 10 km or finer that start to resolve motions in the meso-scale regime.

Spurious, dispersive phenomena are a common problem inherent to computational fluid dynamics. Examples include the Gibbs phenomenon, non-propagating numerical modes and spectral blocking (e.g. Rood (1987)). These phenomena may propagate, interact nonlinearly and negatively impact the model solution. An economic method to reduce these dispersive modes is to add an explicit diffusion term to the equations of motion prior to discretization. Most often, a hyper-diffusion technique is used as documented in Jablonowski and Williamson (2011). This provides a mechanism to dissipate these known spurious modes, presumably, before they have a negative impact on the overall dynamics.

Generally, the strength of the diffusive process is empirically tuned so that the kinetic energy spectra imitate observation (Boville 1991; Takahashi et al. 2006). This technique is classically utilized in spectral transform based schemes where the Gibbs phenomenon is

present when sharp gradients in the flow field arise. Explicit diffusion or filtering processes are also widely used in finite-difference or spectral element dynamical cores. In contrast, flux-limiting finite-difference and flux- or slope-limiting finite-volume methods typically introduce an inherent nonlinear diffusion via the numerical scheme that prevents unphysical oscillations from appearing (Durran 1999). Here, the phrase "unphysical" refers to obvious overshoots and undershoots of numerical estimates. Sometimes the modeler will deliberately choose an inherently diffusive, low-order, numerical scheme to "manage" such numerical issues, and hence avoid or alleviate the need for an additional explicit diffusive term. Considering the treatment of dispersion errors, the management of nonlinear or linear computational instabilities, the effects of grid staggering, and inherent diffusion, all models have some forms of diffusion mechanisms that are not fully grounded in the basic physics of the fluid flow. The overarching goal is to avoid the accumulation of energy or enstrophy at the smallest scales near the truncation limit.

In this paper we explore the linear von Neumann stability characteristics of a second-order and fourth-order horizontal divergence damping mechanism applied on a regular, equal-angle latitude-longitude grid. As a specific instance, we consider the divergence damping implementation in the FV dynamical core of CAM 5 (Lauritzen et al. 2011) which utilizes explicit time-stepping (Neale et al. 2010). The second-order divergence damping mechanism in CAM 5 is also implemented in earlier versions of CAM (CAM 4 and the finite-volume dynamical core in CAM 3.1, see Collins et al. (2004)). This FV dynamical core was developed at the NASA Goddard Space Flight Center, and has some similarities to the Goddard Earth Observing System version 5 model (GEOS5) (Rienecker et al. 2008) and the NOAA Geophysical Fluid Dynamics Laboratory's (GFDL) atmospheric model AM2.1 (Delworth et al. 2006).

The analysis carried out in the following sections is not specific to the finite-volume dynamical core and is relevant to any model that employs divergence damping on a regular latitude-longitude grid with an explicit time-stepping scheme. Our particular analysis is carried out on a staggered D-grid (Arakawa and Lamb 1977). However, the analysis technique generalizes to other grid staggering options and is, in fact, identical for C-grids. We explore the divergence damping mechanism from both a theoretical and practical viewpoint. The latter includes selected dynamical core test cases that demonstrate the impact of the diffusive processes directly on the model simulations. This provides a guiding method to analyze the additional diffusion incorporated in other climate or weather models. Similar tests and analysis can be performed on other forms of explicit diffusion, providing a systematic framework that brings to light the various methods for introducing diffusion to a model. Simulations for two different idealized dynamical core test cases indicate that this linear stability analysis is very accurate, providing more impetus to perform similar stability analyses on other models' methods of explicit diffusion or damping.

This paper is organized as follows. In section 2 we review the finite-volume dynamical core as set up in CAM and discuss the implementation (and motivation) of horizontal divergence damping on a latitude-longitude grid. In sections 3 and 4 we present stability analyses of both the second-order and fourth-order divergence damping mechanisms. In addition, we analyze the impact of various formulations of the divergence damping coefficient on idealized dynamical core simulations and compare these to the theoretical analyses. Conclusions and future work are presented in section 5. The Appendix incorporates the effects of the polar Fourier filter into the stability analyses.

2. The Finite-Volume Dynamical Core in CAM

a. Design aspects

The finite-volume dynamical core in CAM 5 (CAM-FV) is constructed in a flux form which is mass-conserving by design. The hydrostatic approximation allows the horizontal discretization to be built from a 2D shallow water algorithm (Lin and Rood 1997). The vertical discretization of the model utilizes a floating Lagrangian coordinate that is remapped to an Eulerian reference grid after several sub-cycled dynamics time steps (Lin 2004). In this study, we do not directly investigate the effects of this vertical discretization, nor the remapping algorithm. The following is primarily concerned with the horizontal discretization.

The horizontal discretization is based on one-dimensional finite-volume schemes. The prognostic variables are cast on a staggered D-grid that "favors" the conservation of vorticity. In order to compute the mass and momentum fluxes across cell boundaries, a dual C-grid formulation (a "CD" grid) is utilized. First, the variables on the C-grid are advanced by half a time step to estimate the time-centered "advective" C-grid winds. These are then used to advance the prognostic variables on the D-grid which assures a second-order accuracy in time. As an aside, the CD-grid approach introduces some inherent numerical diffusion due to grid interpolations. This is discussed in Skamarock (2008) who reviewed the linear stability characteristics of the CAM-FV dynamical core.

Finite-volume methods are developed with the general supposition that diffusive behavior near steep gradients is preferable to dispersive waves which generate unphysical extrema in the solution (see Bala et al. (2008) for a specific example). CAM 5 primarily uses the for-

mally third-order Piecewise Parabolic Method (PPM, Colella and Woodward (1984)) for the integration of the prognostic variables on the D-grid. In addition, a second-order van Leer method is applied for the computation of the C-grid winds (Lin and Rood 1997). Both algorithms also incorporate a first-order upwind scheme to represent advective inner operators in the cross directions. This approach is designed to eliminate the directional bias or splitting error. However, as pointed out in Lauritzen (2007) this limits the overall accuracy of the entire scheme, introducing nonlinear diffusive effects and possible instabilities. In CAM-FV there are also several choices for the finite-volume slope- and curvature-limiters which are applied near steep gradients (Lin and Rood 1996; Lin 2004). In addition, enhanced inherent diffusion is included near the model top to provide a sponge layer. This is accomplished by lowering the order of the flux operators to a first-order upwind or second-order van Leer scheme and increasing the effects of the divergence damping mechanism in the uppermost few levels (typically 3 levels for a 26-level configuration).

b. *The need for polar filtering*

The Lin-Rood algorithm (Lin and Rood 1997) is developed on a latitude-longitude rectangular grid, with constant (in angle) mesh spacing. This leads to a convergence of the longitudinal (zonal) grid points near each geographic pole. To lessen the corresponding strict time step restriction near the poles, a semi-Lagrangian extension of the transport scheme is implemented in the longitudinal direction (Lin and Rood 1996). However, the semi-Lagrangian method does not filter small-scale noise inherent to this grid and numerical method. Therefore, a polar Fourier filter is applied poleward of the midlatitudes starting

7

at approximately $36 - 40°$ N/S. The Fourier filter coefficients gradually increase in strength as the poles are approached and follow the formulation in Fox-Rabinovitz et al. (1997) (see also Eq. (A1)). The Fourier filter removes linear and nonlinear computational instabilities, but only selectively damps the waves in the zonal direction. No filtering is applied in the meridional direction. It will be shown that the Fourier filter interacts very closely with the horizontal divergence damping discussed in this paper, and both should be considered with some care.

c. Inherent diffusion in CAM-FV

The Lin-Rood algorithm is built to conserve and transport vorticity monotonically. This is done by considering the vector invariant form of the horizontal equations of motion (Lin 2004). Limiters are applied to the vorticity fluxes in a highly nonlinear fashion to ensure that unphysical extrema are not generated. These limiters introduce a certain level of inherent diffusion to the vorticity. This provides, conjecturally, a nonlinear imitation of the kinematic viscosity of a viscous fluid, but does not model the bulk viscosity that appears in divergent flows. As the order of the scheme is increased, this kinematic diffusive process will increase in order which can be concluded from a short calculation of the modified equation for a linear highly simplified flow (not shown here). As an example, the formally third-order PPM scheme corresponds to a fourth-order damping of the vorticity, while the first-order upwind scheme corresponds to a second-order diffusive term. The inherent diffusion in this algorithm is only applied to the vorticity. Divergence damping can therefore be thought of as a "fix" to imitate an equivalent diffusive force on the divergence. Explicitly added horizontal

8

diffusion of the momentum would have the same effect, but would unnecessarily damp the vorticity as well.

The previous discussion may lend an intuitive and qualitative reasoning for the need of divergence damping in CAM-FV, but it does not provide a quantitative method for estimating the needed damping coefficient. Instead, this coefficient intuitively depends on grid size, time step and latitude; that is, physical attributes of the scales of motion. In general, diffusion coefficients are often chosen empirically to match the model with observations and believed "truth". One measure of "truth" is the behavior of the kinetic energy spectrum at large wavenumbers (Nastrom and Gage 1985; Lindborg 1999; Jablonowski and Williamson 2011). This is an indirect measure and should not be used as the sole criterion. As shown in the next section, the choice of the damping coefficient has a significant impact on the dynamics, as a large enough value will introduce instabilities at a fundamental level due to the explicit time-stepping in CAM-FV. Too little damping on the other hand will allow small-scale oscillations to propagate or even fail to prevent instabilities (both linear and nonlinear) from developing.

d. The formulation of horizontal divergence damping

Horizontal divergence damping was suggested by Sadourny (1975), Dey (1978), Haltiner and Williams (1980) and Bates et al. (1993) to control numerical noise in weather forecast models and for numerical stability reasons. The particular form of the second-order

horizontal divergence damping mechanism is

$$\frac{\partial u}{\partial t} = \cdots + \frac{1}{a\cos\phi}\frac{\partial}{\partial\lambda}\left(\nu_2 D\right) \tag{1}$$

$$\frac{\partial v}{\partial t} = \cdots + \frac{1}{a}\frac{\partial}{\partial\phi}\left(\nu_2 D\right), \tag{2}$$

where u and v are the zonal and meridional components of velocity, a is the radius of the earth, $\phi \in [-\pi/2, \pi/2]$ and $\lambda \in [0, 2\pi]$ stand for the latitude and longitude, t is time, and ν_2 symbolizes the second-order divergence damping coefficient. The horizontal divergence D is given by

$$D = \frac{1}{a\cos\phi}\left(\frac{\partial u}{\partial\lambda} + \frac{\partial(v\cos\phi)}{\partial\phi}\right). \tag{3}$$

If we apply the divergence operator to Eqs. (1) and (2) we arrive at the evolution equation for the divergence

$$\frac{\partial D}{\partial t} = \cdots + \nabla^2\left(\nu_2 D\right). \tag{4}$$

This Laplacian type (∇^2) diffusion of the divergence damps all scales, but with more damping at higher wave numbers (akin to the square of the wave number). A standard practice in atmospheric modeling is to invoke a fourth-order hyper-diffusion that is meant to be more scale-selective (fourth power of the wave number, Collins et al. (2004)). This practice is based on the premise that lower-order damping may overly damp the larger scales that are physically relevant, and the presumption that it is the smallest scales that need to be eliminated. Because of this practice, we also explore higher-order damping mechanisms. In particular, the fourth-order divergence damping is given by

$$\frac{\partial u}{\partial t} = \cdots - \frac{1}{a\cos\phi}\frac{\partial}{\partial\lambda}\left(\nu_4\nabla^2 D\right) \tag{5}$$

$$\frac{\partial v}{\partial t} = \cdots - \frac{1}{a}\frac{\partial}{\partial\phi}\left(\nu_4\nabla^2 D\right), \tag{6}$$

10

where ν_4 is the damping coefficient for the fourth-order divergence damping. This leads to the following evolution equation for the horizontal divergence (if we assume that ν_4 has no dependence on ϕ or λ)

$$\frac{\partial D}{\partial t} = \cdots - \nu_4 \nabla^4 D. \tag{7}$$

In the following we perform a linear stability analysis on (4) and (7).

Eq. (4) is easily recognized as the heat (diffusion) equation, and (7) can be seen as the hyper-diffusion equation. Therefore, analyzing the stability of the divergence damping reduces to determining the stability of the diffusion or hyper-diffusion equation on the sphere. The corresponding details of the discretization will likely change somewhat between different model implementations, and this will affect the stability of the scheme; however, the basic analysis should carry over to each individual model. In the following sections we analyze the stability of (4) and (7) using the finite-difference discretization with an explicit time-stepping scheme as implemented in CAM 5. The default CAM 5 configuration employs the second-order divergence damping. The fourth-order damping can be selected as an option at run time. Because we analyze the scalar equations (4) and (7) the nature of the analysis is universal to both the C- and D- grid staggerings, as long as a latitude-longitude geometry is maintained.

3. Second-Order Divergence Damping

a. Stability analysis

For all that follows, subscripts indicate locations on the discretized grid, with the first letter i indicating the east-west (longitudinal or zonal) direction, and the second index j denoting the north-south direction (latitudinal or meridional). $\Delta\lambda$ and $\Delta\phi$ are the constant longitudinal and latitudinal grid spacings, respectively. The divergence damping is applied to the prognostic horizontal wind components that are discretized on the D-grid as discussed above. This is shown in Fig. 1. In this figure the cell is centered at $(i\Delta\lambda, j\Delta\phi)$ and the winds are staggered appropriately around the cell so that the discretized vorticity $\zeta_{i,j}$ lies at the cell center. This places the divergence at the cell corners as illustrated in Fig. 1.

The divergence of the flow field with

$$u_{i,j-1/2} = u\left(i\Delta\lambda, (j-1/2)\Delta\phi\right)$$

$$v_{i-1/2,j} = v\left((i-1/2)\Delta\lambda, j\Delta\phi\right),$$

is given by

$$D_{i-1/2,j-1/2} = \frac{1}{a\cos\phi_{j-1/2}}\left[\frac{u_{i,j-1/2} - u_{i-1,j-1/2}}{\Delta\lambda} + \frac{v_{i-1/2,j}\cos\phi_j - v_{i-1/2,j-1}\cos\phi_{j-1}}{\Delta\phi}\right]. \quad (8)$$

We then write the discretized versions of Eqs. (1) and (2) as follows (the superscript 'n' refers to the time index, i.e. $\chi_{i,j}^n = \chi(i\Delta\lambda, j\Delta\phi, n\Delta t)$):

$$\frac{u_{i,j-1/2}^{n+1} - u_{i,j-1/2}^n}{\Delta t} = \frac{\nu_2}{a\Delta\lambda\cos\phi_{j-1/2}}\left[D_{i+1/2,j-1/2}^n - D_{i-1/2,j-1/2}^n\right]$$

$$\frac{v_{i-1/2,j}^{n+1} - v_{i-1/2,j}^n}{\Delta t} = \frac{\nu_2}{a\Delta\phi}\left[D_{i-1/2,j+1/2}^n - D_{i-1/2,j-1/2}^n\right].$$

Note that we have assumed that the coefficient ν_2 is independent of ϕ and λ (in reality we only need to assume that $\cos \phi$ does not vary on the grid level, as discussed below). In practice, ν_2 is chosen to be dependent on the time-step Δt and grid spacing (possibly latitudinally dependent). Suppression of this dependence at this point simplifies the algebra. Ideally we want to analyze the stability of this system, however this becomes prohibitive, as the eigenvalues inherent to the problem are not conducive to calculation. Instead we consider the evolution of the divergence (Eq. (4)) in CAM-FV which is discretized with the finite-difference approach

$$
\begin{aligned}
&\frac{D_{i-1/2,j-1/2}^{n+1} - D_{i-1/2,j-1/2}^{n}}{\Delta t} \\
&= \frac{\nu_2}{a^2 \cos \phi_{j-1/2}} \left\{ \frac{\cos \phi_j \left(D_{i-1/2,j+1/2}^n - D_{i-1/2,j-1/2}^n \right) - \cos \phi_{j-1} \left(D_{i-1/2,j-1/2}^n - D_{i-1/2,j-3/2}^n \right)}{(\Delta \phi)^2} \right. \\
&\left. + \frac{D_{i+1/2,j-1/2}^n - 2 D_{i-1/2,j-1/2}^n + D_{i-3/2,j-1/2}^n}{(\Delta \lambda)^2 \cos \phi_{j-1/2}} \right\}. \quad (9)
\end{aligned}
$$

The same analysis holds on the C-grid if each of the indices above are shifted by $1/2$, not affecting the results obtained below.

In practice the divergence damping coefficient is defined as

$$
\nu_2 = C_2 \, \cos^r \phi \, \frac{a^2 \Delta \phi \Delta \lambda}{\Delta t}, \quad (10)
$$

where $r = 0$ is the default in CAM 5.0. The parameter r can be chosen to modify the latitudinal dependence of the damping coefficient. The empirical "tuning" parameter C_2 depends on the position in the vertical direction to provide increased damping near the model top. More information on C_2 is provided below. This formulation of ν_2 with $r = 0$ is proportional to the area of a grid cell at the equator, and inversely proportional to the time step. Dimensionally this is an appropriate choice of damping coefficient, however reliance

13

on the area of the grid cell at the equator, and not the true area of the grid cell (with appropriate latitudinal dependence) places the same damping effect on a given physical wave-length, regardless of discretization or latitudinal location.

Using (10) we now assume that $\cos\phi$ is approximately constant at the grid level ($\cos\phi_{j+1} \sim \cos\phi_j \sim \cos\phi$, which is the same approximation alluded to in deriving the evolution of the divergence). We consider a standard von Neumann stability analysis of Eq. (9), following Lauritzen (2007). In Lauritzen (2007) the discretization was formulated as a cell average approach. This is identical to the above, if we simply replace each $D_{i-1/2,j-1/2}$ with the corresponding cell average at each grid cell. Hence, we consider the growth of each wave number k (or combination of longitudinal and latitudinal wave numbers k_λ and k_ϕ in this case) by looking at solutions of the type

$$
\begin{aligned}
D(\lambda,\phi,t) &= D_0 e^{\imath\left(\omega t + k_\lambda\lambda + k_\phi\phi\right)} \\
\Rightarrow D_{i,j}^n &= D_0 \Gamma_2^n e^{\imath(ik_\lambda\Delta\lambda + jk_\phi\Delta\phi)},
\end{aligned}
\tag{11}
$$

where D_0 denotes the initial amplitude of the wave, ω stands for the frequency, $\Gamma_2 = e^{\imath\omega\Delta t}$ is the complex amplification factor, and $\imath = \sqrt{-1}$ represents the imaginary unit number. The scheme described previously is stable if the growth in each wave number, given by $|\Gamma_2|$, is less than or equal to unity (although a more realistic restriction is to force Γ_2 to remain positive as well). Inserting the ansatz (11) in the discretized divergence equation (9), and dividing by the common factor $D_0\Gamma_2^n e^{\imath\left[(i-1/2)k_\lambda\Delta\lambda + (j-1/2)k_\phi\Delta\phi\right]}$ we identify the amplification factor as

$$
\Gamma_2 = 1 - 4\,C_2\,\cos^r\phi\left\{\alpha\sin^2\left(\frac{k_\phi\Delta\phi}{2}\right) + \frac{1}{\alpha\cos^2\phi}\sin^2\left(\frac{k_\lambda\Delta\lambda}{2}\right)\right\},
\tag{12}
$$

where $\alpha = \Delta\lambda/\Delta\phi$ is the grid aspect ratio. Note that Eq. (12) is real because this dis-

cretization is symmetric. In our model simulations, α will be identical to 1. In default CAM 5 configurations an aspect ratio of $\alpha \sim 1.33$ is also often chosen with wider longitudinal grid spacings.

As mentioned, the minimum requirement for stability in a linear flow is to restrict C_2 such that $|\Gamma_2| \leq 1$, although it would be preferable to restrict $0 \leq \Gamma_2 \leq 1$ ensuring that the modes do not change sign with each time step. At the equator with $\phi = 0°$, these requirements are equivalent to

$$C_2 \left\{ \alpha + \frac{1}{\alpha} \right\} \leq \frac{1}{4} \qquad \text{and} \qquad C_2 \left\{ \alpha + \frac{1}{\alpha} \right\} \leq \frac{1}{8},$$

where the stricter requirement does not allow the sign of the wave to change with each time step. However, near the poles Eq. (12) becomes increasingly more restrictive, indicating that instabilities in the divergence field will emerge in the polar regions (particularly for $r = 0$). Note that this singularity appears in the zonal direction as the poles are approached $(|\phi| \to \pi/2)$ and originates from the second term in the curly brackets in Eq. (12). The polar Fourier filter is designed to remove zonal instabilities near the poles, and so in practice this instability is not revealed in CAM-FV. To see how the polar Fourier filter removes this instability, the reader is referred to the Appendix.

While the singularity at the poles found in (12) for $r = 0$ is controlled by the polar filter, it is of interest to consider $r = 1$ as well, which takes the latitudinal dependence of the grid cell's approximate area into account. In this instance, the singularity in the zonal direction is reduced near the poles, but now there is an additional $\cos \phi$ on the meridional modes (first term in the curly bracket in (12)) which reduces the effective damping of such modes near the poles. In essence, this indicates a delicate balance between the zonal and meridional waves;

15

using $r = 0$ damps the wave numbers in the meridional direction sufficiently, but is only marginally stable (with the application of the Fourier filter) for the zonal wave numbers, while using $r = 1$ reduces this instability in the zonal direction, but does not damp the meridional waves as efficiently. To visualize these effects, Fig. 2 provides a plot of the amplification factor Γ_2 (without Fourier filter) for both $r = 0$ (CAM default) and $r = 1$ at a latitude of $\phi = 60°$. The top row is shown for the typical CAM 5 values of $C_2 = 1/128$ and $\alpha = 1.33$, the bottom row displays the extreme case (critical at the equator at least) $C_2 = 1/4$ with $\alpha = 1$. These constant C_2 values neglect the sponge layer at the model top that is discussed later. Note that the axis labels are described by $x = k_\lambda \Delta\lambda$ and $y = k_\phi \Delta\phi$ where the value of x=y=π denotes the smallest wavelength $2\Delta\lambda$ or $2\Delta\phi$.

At this latitude of $\phi = 60°$ the typical CAM 5 configurations (Figs. 2(a,b), (b) is the default) are stable since the amplification factors are bounded by $|\Gamma_2| \leq 1$. However, there is a latitude close to the poles for which both $r = [0, 1]$ become unstable. In particular, the instability occurs when the $(2\Delta\lambda, 2\Delta\phi) = (\pi, \pi)$ wave drops below -1. For $r = 1$ this does not occur until $|\phi| > 89°$ (not shown). For $r = 0$ the amplification drops below -1 for $|\phi| > 83°$. Both instabilities are adequately controlled by the polar Fourier filter, as illustrated in the Appendix.

The key observation to take away from Fig. 2 is that at these higher latitudes the waves in the zonal direction become unstable, while for $r = 1$, the purely meridional wave numbers become less damped with increasing wavenumber (decreasing scale). This can partially be seen from Fig. 2c where we observe that the $2\Delta\phi$ wave $(0, \pi)$ has an amplification factor of $\Gamma_2 \sim 0.8$ for $r = 1$, whereas the corresponding amplification factor for $r = 0$ is $\Gamma_2 \sim 0.4$ (Fig. 2d). This implies that at high latitudes (here $\phi = 60°$), using $r = 1$ will not quickly

damp out small-scale purely meridional waves. However, as noted in the previous paragraph, the choice of $r = 0$ implies that the polar filter is required to maintain the computational stability at a lower latitude than would be needed for $r = 1$.

b. Vertical Profile of the second-order damping coeffcient

As mentioned previously, the parameter C_2 is designed to depend on the vertical position in the FV dynamical core. This dependence introduces a diffusive sponge layer near the model top to absorb rather than reflect outgoing gravity waves. This concept of a diffusive sponge layer is outlined in Jablonowski and Williamson (2011). The use of sponge layers has come under questioning (Shepherd et al. 1996) as it also introduces an artificial sink for momentum, and some nonlinear transfer of energy takes place due to the total energy fixer employed by all default versions of CAM (Neale et al. 2010). The purpose of this discussion is to determine the characteristics that arise when utilizing an artificially determined sponge layer for the divergence damping, as employed in CAM 5 and its predecessor versions CAM 4 and CAM-FV 3.1.

In the following we rely on the discussion in the previous section, with all the same definitions. Let p_{top} be the pressure at the model top (in most default CAM runs this is taken to be $p_{top} \sim 3$ hPa) and let p^l_{ref} be the reference pressure at a given model level with index l. The computation of p^l_{ref} is based on the definition of the hybrid η-coordinate (see also Collins et al. (2004)) and assumes a surface pressure of 1000 hPa. Then, as implemented in the FV dycore, the parameter C^l_2 depends on the model level and is given by

$$C^l_2 = c \max \left\{ 1, 8 \left[1 + \tanh \left(\ln \left(\frac{p_{top}}{p^l_{ref}} \right) \right) \right] \right\}. \tag{13}$$

The default value for c is $1/128$ which (modulo the $\cos\phi$) is certainly within the stable range at most latitudes determined in the previous section. For typical model runs this provides a rather flat vertical profile until the final two to three model levels, whereupon the damping coefficient is increased rapidly by up to a factor of 8. It means that the strength and frequency of the polar instabilities increase near the model top due to this increased damping coefficient, requiring a stronger diffusive fixer to remove them, perhaps in addition to the polar Fourier filter. Such a fixer is, possibly serendipitously, already in place in the form of lowering the order of the numerical scheme near the model top. The latter aspect is a specific attribute of CAM-FV, i.e., this result is implementation-dependent.

Investigating the functional dependence of (13) on the location of the model top also raises another issue. Most model runs will be performed with the model top prescribed near $2 - 3$ hPa, however test cases specifically designed to test the dynamical core (Jablonowski et al. 2008a) lower the model top so as to highlight different aspects of the model's numerics. One such instance is a gravity wave test case without the Earth's rotation and an initial state at rest in which the squared Brunt-Vaisala frequency of the hydrostatic background conditions is prescribed as $N^2 = 10^{-4}$ s^{-2}. An overlaid potential temperature perturbation then triggers the propagation of gravity waves. The surface temperature and pressure are set to 300 K and 1000 hPa, respectively. With a constant (in height) vertical grid spacing of $\Delta z = 500$ m and 20 vertical levels (L20), this forces the pressure at the model top to be $p_{top} = 273$ hPa. The dependence of the multiplicative factor C_2 on the position of such a rather high (low-lying) p_{top} value is illustrated in Fig. 3. The figure depicts the vertical profile of C_2 (Eq. (13)) for a model top at 3 hPa (solid line) and 273 hPa (dashed line). When the model top is lowered to 273 hPa the damping strengthens throughout the entire

18

model, but particularly at the upper levels. This leads to not just a sponge layer, but an entire spongy model, detrimentally affecting the outcome of the gravity wave test case.

This observation explains a result by Jablonowski et al. (2008b) that compared the CAM-FV simulations to several other dynamical cores at their default configurations. It was noted that the default CAM-FV dynamical core with second-order divergence damping appeared to be extremely diffusive for this test case. Figure 4 displays this result. It depicts the potential temperature perturbation ($\Theta' = \Theta - \overline{\Theta}$) along the equator from the zonally symmetric initial state $\overline{\Theta}$, after the wave has developed for 96 hours. Note that there is a significant difference in the Θ' amplitudes and gradients between the $1° \times 1°$ L20 CAM-FV simulation with default divergence damping (Fig. 4a) and no divergence damping (Fig. 4c). For comparison, Figs. 4b,d display the corresponding results of an alternative CAM dynamical core which is the spectral transform Eulerian (CAM-EUL) model (Collins et al. 2004). It is run at a comparable resolution with the triangular truncation T85 and the identical 20 levels. In Fig. 4b the CAM-EUL default fourth-order hyper-diffusion with the coefficient $K_4 = 1 \times 10^{15}$ m^4 s^{-1} is used, in addition to a second-order diffusive sponge layer at the top with the base coefficient $K_2 = 2.5 \times 10^5$ m^2 s^{-1}. In (d) both the CAM-EUL K_2 and K_4 coefficients were set to zero.

Figure 4 showcases several effects. First, the divergence damping in Fig. 4a significantly suppresses the evolution of the gravity wave along the equator and also seems to introduce a positive potential temperature perturbation in CAM-FV at the model top (near 180°). Secondly, the shape of the gravity waves in CAM-FV appear to be influenced by both the explicit diffusion via divergence damping (Fig. 4a) as well as the intrinsic diffusion via the numerical scheme (Fig. 4c). The latter can be concluded when CAM-FV is compared to

CAM-EUL. The EUL simulations are characterized by sharper Θ' gradients at the leading edge of the gravity wave, even when hyper-diffusion is applied in the simulation (Fig. 4b). However, the perturbation amplitudes in the simulations without explicitly added damping (Figs. 4(c,d)) are comparable in both models. As an aside, omitting the explicit damping in CAM-FV and CAM-EUL is only feasible in idealized test cases such as the gravity wave test described here. It truly isolates the effects of the damping. In practical applications though, the damping is needed to avoid an accumulation of energy at the smallest scales and prevent CAM-EUL from becoming unstable.

4. Fourth-Order Divergence Damping

a. Stability analysis

Higher-order forms of divergence damping act more strongly on the higher wave numbers, while limiting the effects on the large-scale well-resolved features of the flow. We now analyze the stability constraints for fourth-order divergence damping using the notation introduced in section 3.

As before, we analyze the scalar equation (7) which we discretize with the help of (8) and the following expression for the Laplacian of the divergence (also refer to Fig. 1)

$$
\begin{aligned}
&\left(\nabla^2 D\right)_{i-1/2,j-1/2} \\
&= \frac{D_{i+1/2,j-1/2} - 2D_{i-1/2,j-1/2} + D_{i-3/2,j-1/2}}{a^2 \left(\Delta\lambda\right)^2 \cos^2 \phi_{j-1/2}} \\
&+ \frac{\left(D_{i-1/2,j+1/2} - D_{i-1/2,j-1/2}\right) \cos \phi_j - \left(D_{i-1/2,j-1/2} - D_{i-1/2,j-3/2}\right) \cos \phi_{j-1}}{a^2 \left(\Delta\phi\right)^2 \cos \phi_{j-1/2}}.
\end{aligned}
\tag{14}
$$

It yields the discretized version of (7)

$$
\begin{aligned}
\frac{D^{n+1}_{i-1/2,j-1/2} - D^{n}_{i-1/2,j-1/2}}{\Delta t} &= -\frac{\nu_4}{a^2 \cos\phi_{j-1/2}} \left\{ \frac{\cos\phi_j}{(\Delta\phi)^2} \left[\left(\nabla^2 D^n\right)_{i-1/2,j+1/2} - \left(\nabla^2 D^n\right)_{i-1/2,j-1/2} \right] \right. \\
&\quad - \frac{\cos\phi_{j-1}}{(\Delta\phi)^2} \left[\left(\nabla^2 D^n\right)_{i-1/2,j-1/2} - \left(\nabla^2 D^n\right)_{i-1/2,j-3/2} \right] \\
&\quad \left. + \frac{\left(\nabla^2 D^n\right)_{i+1/2,j-1/2} - 2\left(\nabla^2 D^n\right)_{i-1/2,j-1/2} + \left(\nabla^2 D^n\right)_{i-3/2,j-1/2}}{(\Delta\lambda)^2 \cos\phi_{j-1/2}} \right\}.
\end{aligned}
\tag{15}
$$

Here we again assume that ν_4 does not depend on ϕ or λ. While this is not entirely accurate in CAM-FV, it is permissible because we also make the assumption that $\cos\phi$ does not change on the grid level.

To analyze the stability of Eq. (15), we consider solutions of the form (11). The fourth-order damping coefficient ν_4 in CAM 5 is defined as

$$
\nu_4 = C_4 \frac{a^4 (\Delta\lambda)^2 (\Delta\phi)^2 \cos^r \phi}{\Delta t},
\tag{16}
$$

where $r = 2$ (the CAM 5 default if the optional fourth-order damping is invoked) lets ν_4 vary as the square of the area of each grid cell (dependent on latitude or $\cos\phi$ which again is assumed constant at the grid level). In CAM 5, the parameter C_4 is set to a default value of 0.01. Note that ν_4 does have a latitudinal dependence, but for the local analysis considered here with an approximately constant $\cos\phi$ at the grid level we can use (7). Once again we desire the modulus of the amplification factor $|\Gamma_4| = |e^{\iota\omega\Delta t}|$ to have magnitude less than or equal to unity. Γ_4 is found to be

$$
\Gamma_4 = 1 - 16\, C_4 \cos^r \phi \left\{ \alpha \sin^2\left(\frac{k_\phi \Delta\phi}{2}\right) + \frac{1}{\alpha \cos^2\phi} \sin^2\left(\frac{k_\lambda \Delta\lambda}{2}\right) \right\}^2,
\tag{17}
$$

where $\alpha = \Delta\lambda/\Delta\phi$ as before. The effect of the polar Fourier filter on the amplification factor, and the corresponding stability constraint are described in the Appendix.

At the equator with $\phi = 0°$ the stability constraint $|\Gamma_4| \leq 1$ implies that C_4 needs to be less or equal $1/32$. However, the more conservative (and more desirable) constraint $0 \leq \Gamma_4 \leq 1$ demands the more restrictive bound $C_4 \leq 1/64$. Both values are quoted for $\alpha = 1$ and $r = 2$. The first estimate of the maximal value of C_4 is experimentally confirmed by considering baroclinic wave tests with CAM 5. This baroclinic wave test for dynamical cores is described in Jablonowski and Williamson (2006a,b). In essence, a perturbation in the zonal wind is added to a steady-state flow field that is initially in gradient-wind and hydrostatic balance. This perturbation develops into a baroclinic wave in the northern hemisphere. The wave breaks after nine days and creates sharp temperature fronts. However prior to day 5, the flow is primarily linear, and hence amenable for comparisons to the linear analysis performed here.

Leaving all other parameters fixed, the parameter C_4 was adjusted near the maximal value of $1/32$ for the baroclinic wave. It was found that the evolution of the baroclinic wave with $C_4 < 0.031$ remained stable, whereas the model quickly developed numerical instabilities when C_4 exceeded this critical value. The simulation blew up after a few model hours. Figure 5 shows this development for $C_4 = 0.031$ after 4 hours and 45 minutes in the baroclinic wave test case at the resolution $1° \times 1°$ with 26 levels. Here, the vertical pressure velocity at the model level near 867 hPa is depicted. A similar situation developed for the gravity wave test (not shown). The instability develops in the $(2\Delta\lambda, 2\Delta\phi) = (\pi, \pi)$ wave.

Note that the instability in Fig. 5 develops near $\phi \sim 36°N$ which is precisely the position where the polar Fourier filter begins to take effect (with $\alpha = 1$). This also explains the slight discrepancy between the predicted value of $1/32 = 0.03125$ and 0.031 as observed in the model runs. If the previously omitted grid-level latitudinal dependence of Γ_4 is taken

into account, an instability is expected to develop at almost exactly $C_4 = 0.031$ for $\phi = 36°$. Poleward of this latitude the polar Fourier filter removes the zonal portion of this instability, and evidently controls its development. Eventually however, the developing instability at $36°$ overcomes the polar filter, and cascades throughout the model.

The relaxed bound $C_4 \leq 1/32$ allows the solution to change sign at each time step. Therefore, we expect that this constraint would not be sufficient for a more realistic, nonlinear flow. Instead, the more conservative restriction $C_4 < 1/64 = 0.015625$ (for $\alpha = 1$) is recommended, which is quite close to the CAM 5 default value of $C_4 = 0.01$. For the default CAM-FV settings where $\alpha = 1.33$, the recommended restriction at the equator is $C_4 < 9/625 = 0.0144$ according to Eq. (17).

b. *Latitudinal dependence and meridional waves*

Figure 6 illustrates how Γ_4 (without applying the Fourier filter) with $r = 2$ depends on latitude and shows the amplification factors at both the Fig. 6(a,c) equator and Fig. 6 (b,d) $|\phi| = 60°$. Both the Fig. 6(a,b) CAM 5 default configuration as well as the Fig. 6(c,d) extremal cases are depicted. At higher latitudes Fig. 6(b,d), Γ_4 is smaller for the smallest zonal wave numbers ($x = \pi$). $\Gamma_4 < -1$ indicates the appearance of the grid-induced instability. For the extremal case ($\alpha = 1, C_4 = 1/32$), this happens for any latitude away from the equator. In contrast, for the default CAM-FV settings of $C_4 = 0.01$ and $\alpha = 1.33$ this occurs for $|\phi| > 76°$. This lies in the region where the Fourier filter is active.

Figure 6 demonstrates that the $\cos^r \phi$ (with default $r = 2$) dependence of the meridional wave modes (first term in the curly bracket in Eq.(17)) causes the purely meridional waves

$(0, y)$ to be damped very little at high latitudes. In particular, Figs. 6(b,d) show that the purely meridional $2\Delta y$ (or $(0, \pi)$) wave is hardly damped at all at $\phi = 60°$. While this does not introduce an instability, it does not quickly remove the high-order modes either. This can be confirmed by analyzing model runs of the baroclinic wave test in Fig. 7. The figure shows the vertical pressure velocity at the model level near 867 hPa at day 4 in CAM-FV for both the second-order (top row) and fourth-order (bottom row) divergence damping mechanism. Both the default CAM 5 damping coefficients (left column) and runs with doubled coefficients (right column) are depicted. The careful consideration of this test case indicates that a meridional wave is triggered shortly after the initialization, with wavelength around 6°. For the depicted $1° \times 1°$ grid spacing, this corresponds to $(0, \pi/3)$ in Figs. 2 and 6. Figure 7 illustrates the persistence of these waves in the vertical pressure velocity despite a doubling in the magnitude of the damping coefficients. The default second-order damping does not remove these waves either, but a simple doubling of the coefficient C_2 removes most of their effects. However, this comes at the cost of damping the resolved large-scale signal as well which might be unacceptable from a physical viewpoint.

To understand the damping characteristics at the equator, we can evaluate the amplification factors (12) and (17) for this particular example with $\alpha = 1$. For the default CAM-FV values $C_4 = 0.01$ and $C_2 = 1/128$ with a meridional wavelength of 6° the amplification factors are $\Gamma_4 = 0.99$ and $\Gamma_2 = 127/128 = 0.9921875$. If the 6° wave is introduced at time step $n = 0$, then it would take approximately until $n = 70$ and $n = 90$ time steps for the fourth-order and second-order damping to damp the wave to half its original amplitude, respectively. When the damping coefficients are doubled as displayed in Fig. 7 (right column) this corresponds to $\Gamma_4 = 0.98$ and $\Gamma_2 = 63/64 = 0.984375$. These values require approx-

24

imately $n = 35$ and $n = 45$ time steps for the fourth-order and second-order divergence damping to reduce the wave's amplitude by half (at the equator).

The apparent inability of divergence damping, and in particular fourth-order divergence damping, to adequately damp these small-scale modes is not immediately intuitive. An understanding can be gained by again considering Fig. 6. Note that along the line $x = 0$ the damping coefficients for both forms of damping is maximal, i.e. the amplification factor at $(0, y_0)$ is greater than at (x, y_0) for any $x \neq 0$. Physically this means that of all the modes damped by divergence damping, the purely meridional waves will be damped the least, whereas modes with mixed directions will be damped more adequately.

To understand why the second-order damping is more effective at removing these purely meridional waves, we must consider the effect that changes in latitude have on the amplification factors. Using the example from above but now at the high latitude of $\phi = \pi/3 = 60°$, the amplification factor for the 6° purely meridional wave is $\Gamma_4 = 0.9975$ which requires $n = 280$ time steps to damp the wave adequately for the default value of $C_4 = 0.01$. When using $C_4 = 0.02$, the amplification factor is $\Gamma_4 = 0.995$ which requires approximately $n = 140$ time steps to halve the amplitude of the 6° purely meridional wave. The second-order divergence damping employed in the runs illustrated in Fig. 7 (bottom row) uses Eq. (10) so that the amplification factor for purely meridional waves are independent of latitude, and thus only require approximately $n = 90$ or $n = 45$ time steps for $c = 1/128$ and $c = 1/64$ to reduce the amplitude by half. Hence, it is this latitudinally dependent weakening of the fourth-order damping that allows the meridional waves to remain undamped for so long. In an effort to efficiently remove these modes and to obtain a damping coefficient meant to damp physical modes of a given size, regardless of latitudinal location and resolution, a

modified fourth-order damping coefficient with $r = 0$ could be considered.

While it is not likely that such a modified formulation completely eliminates the meridional waves displayed in Fig. 7, it should damp these waves more effectively than the previous formulation. However one can also notice that the instability present at $k_\lambda \Delta\lambda = \pi$ and $k_\phi \Delta\phi = \pi$ will then be stronger in this case. This $1/\cos^4 \phi$ instability near the poles will be stronger than the polar Fourier filter is designed to remove, so additional application or strengthening of the Fourier filter would be required. This is due to the current formulation of the damping coefficients in the Fourier filter itself. The coefficients (Eq. (A1)) are proportional to $\cos^2 \phi$, and can remove an instability in the zonal direction that depends on $1/\cos^2 \phi$ which is the case for $r = 2$. Γ_4 with $r = 0$ presents a unique problem in that there is an additional $1/\cos^2 \phi$ instability in the mixed direction, i.e. it is no longer the case that only zonal wave numbers become unstable near the poles. This implies that a simple application of the Fourier filter may not be sufficient to maintain stability.

c. Direct comparison of second-order and fourth-order divergence damping

As a final summary, Fig. 8 provides a direct comparison of the second- and fourth-order damping characteristics with the amplification factors Γ_4 with $r = 2$, and Γ_2 with $r = 0, 1$ at the (a,c) equator and (b,d) $|\phi| = 60°$. The amplification factors are plotted for identical wave numbers in both directions along the x-axis where Δx is a placeholder for both $\Delta\lambda$ and $\Delta\phi$. In Figs. 8a,b the default CAM 5 Γ_4 and Γ_2 formulations with $C_4 = 0.01, r = 2$ and $C_2 = 1/128, r = 0$ are compared for the default aspect ratio $\alpha = 1.33$. In addition, Figs. 8c,d compare the extremal values (region of marginal stability at the equator) with aspect

ratio $\alpha = 1$ for Γ_4 with $C_4 = 1/32, r = 2$ and Γ_2 with $C_2 = 1/4, r = 1$. The reason for evaluating the latitudinally dependent $r = 1$ case for the second-order damping instead of the default $r = 0$, is because the fourth-order divergence damping with $r = 2$ has the same area-dependence of the damping coefficient built-in.

Figures 8a,b show that the fourth-order damping is significantly stronger at the smallest scales. However, any amplification factor below 0.95 damps out the specified modes very effectively for long-term simulations since the damping is applied at each time step. Therefore, the damping rates of 0.3 or 0.85 in (b) for the $2\Delta x$ mode are not very different from each other in long climate runs. In general, we see that both forms of damping effectively eliminate the small-scale features such as the 2, 3, 4 Δx waves. The difference in the speed of the removal is evident, but is expected to play a minor role in climate simulations. However, this difference is important for data assimilation applications similar to the ones employed by the CAM Data Assimilation Research Testbed (CAM-DART) (Anderson et al. 2009) where the unbalanced nature of the model repeatedly introduces small-scale waves that must be damped out quickly. For this application of CAM (as well as for numerical weather prediction) the fourth-order damping mechanism is much more effective at small scales, while hardly influencing the well-resolved wave modes. This, combined with our observations for the purely meridional waves, explains recent observations that CAM-DART with fourth-order divergence damping adequately removes small-scale waves in the zonal direction (which is not the case for second-order damping), but maintains some noisy meridional waves in the polar regions (Lauritzen et al. 2011).

Figure 8b also shows that for modes larger than $6\Delta x$ the second-order divergence mechanism at $\phi = 60°$ becomes stronger than the fourth-order scheme. The damping is only slightly

27

stronger, but since the effect of the amplification factor is exponentially scaled, small differences near unity have major impact. In addition, these scales are well-resolved and have physical relevance. If the second-order mechanism damps them more, the effects are more likely to be evident in simulations. Overall, the fourth-order divergence damping or even high-order damping schemes are more scale-selective and more aggressive at removing the smallest scale waves while providing less damping at the larger modes. On the downside, higher-order schemes lead to a very restricted region of stability when applied in explicit time-stepping schemes.

Figures 8c,d clearly show for the extreme case that the fourth-order divergence damping barely damps the longer wavelengths until they reach $10\Delta x$ size. In contrast second-order divergence damping damps all modes except those of the very largest wavelength. The strongly negative values (< -1) of the amplification factors in Fig. 8d are not necessarily a concern as this choice of C_4 lies at the edge of the equatorial stability region and should not be used in practice for high latitudes. Instead, plots (c) and (d) are meant to only illustrate the qualitative behavior of the two damping mechanisms.

Fourth-order divergence damping is implemented as an option not only in CAM 5, but also in other GCMs such as the forthcoming GFDL/NASA finite-volume dynamical core on a cubed-sphere grid (Putman and Lin 2009). Even sixth- and eigth-order divergence damping mechanisms have been tested with the finite-volume algorithm on the cubed-sphere grid (S.-J. Lin and W. Putman, personal communication, 2010). Note that the cubed-sphere grid does not suffer from the convergence of the meridians, or equivalently discretization on the grid avoids the $1/\cos\phi$ singularity that appears in this analysis. The intent of the damping mechanisms is to remove small-scale waves to prevent an accumulation of energy

28

at the smallest scales. The singularity introduced by the latitude-longitude grid at the poles forces a trade-off between instabilities at the smallest resolvable scale $(2\Delta\lambda, 2\Delta\phi)$ and the inability of the damping to efficiently remove small-scale meridional waves. With the latitude-longitude grid, there is no clear winner, and while it may seem more acceptable to retain small-scale meridional waves longer than desired, as opposed to the introduction of grid-scale instabilities, this raises the question whether or not the fourth-order damping is truly damping sufficiently.

5. Conclusions

A linear von Neumann analysis is applied to the divergence damping implemented in CAM 5. Although care is taken to follow definitions and notation used within the CAM-FV framework, the analysis performed is not specific to CAM-FV. This analysis is specific only to divergence damping applied on a latitude-longitude grid with an explicit time-stepping scheme. This type of analysis can easily be adapted to other models, especially to those on other rectangular grids.

Stability restrictions are derived for both the second- and fourth-order divergence damping coefficients with homogeneous (in angle) grid spacing. While these restrictions are valid at the equator, the general formulas for the amplification factors provide the freedom to consider restrictions at other latitudes. In addition, the stability constraint depends on the grid resolution aspect ratio α which is accounted for in the derivation. All model simulations utilized an equal grid spacing in both horizontal directions with $\alpha = 1$. The paper also demonstrates that different values of α alter the derived stability restriction.

The vertical dependence of the second-order divergence damping in CAM-FV is investigated. While most model runs with typical pressure values of 2-3 hPa at the model top are not negatively affected by the artificial 'sponge layer', it adequately explains the diffusive characteristics of idealized CAM-FV simulations with low-lying model tops around $p_{top} = 273$ hPa. In general, the effect of a sponge layer on the model needs to be carefully considered, as near the poles this sponge layer becomes increasingly unstable, and can become a source of divergence, rather than a sink of it.

The validity of the derived stability restrictions on the damping coefficients is experimentally confirmed through gravity wave and baroclinic instability tests of CAM-FV. The dynamical core simulations indicate that the analysis is very accurate for linear flows. The theoretical analyses and model simulations suggest that the fourth-order divergence damping parameter should be restricted by $C_4 \leq 1/64$ for $\alpha = 1$ and $C_4 \leq 9/625$ for the CAM 5 default $\alpha = 1.33$ setting. In addition, the latitudinal dependence of the damping has been investigated. For the fourth-order divergence damping it is found that the control of the grid-inherent singularity at the pole sacrifices the efficient reduction of small-scale purely meridional waves. Employing a damping coefficient that neglects the latitudinal variation of the grid cell area will likely damp these meridional waves more effectively, but the polar singularity will then be more apparent.

Most of the issues raised in this paper appear to be dependent on the choice of the computational grid. This analysis quantifies part of the effect that the two singular poles in a latitude-longitude grid have on the subgrid-scale dynamics. In order to extend this analysis, the same method will be applied to other grid formulations, such as the finite-volume cubed-sphere dynamical core which is in development at GFDL and NASA. While

this grid is presumably an improvement over the latitude-longitude grid, it also has its own peculiarities that must be accounted for in an analysis of the divergence damping.

Other sources of diffusive behavior in CAM-FV or other GCMs include inherent numerical diffusion, the use of 'sponge layers' at the model top, and filters and fixers that are meant to remove spurious waves that do not have physical origin. This paper quantifies the effect of one of these processes on the dynamics of a GCM. As illustrated, the divergence damping introduced to maintain numerical stability has the potential to introduce instability which negates the intended effect. Careful consideration of these processes should be high priority in the development of future models, so that their spurious impact on climate or weather predictions can be minimized.

APPENDIX

Incorporating the Polar Fourier Filter

We include the effect of the polar Fourier filter in the derivation of the amplification factors Γ_4 and Γ_2. The discretization provided in CAM 5 applies the filter only to the time tendencies of the winds, and not directly to the prognostic variables. For our analysis of the divergence equation this is equivalent to considering the update equation of the divergence (without any filtering) as

$$\frac{D_{i,j}^{n+1} - D_{i,j}^n}{\Delta t} = \beta_{i,j}^n$$

where β represents the 'tendency' of the divergence. For a von Neumann stability analysis, one considers the Fourier decomposition of the discrete equation, which for the tendency can be written as

$$\beta_{i,j}^n = \sum_{k_\lambda, k_\phi} \tilde{b}_{k_\lambda, k_\phi} e^{-\imath(k_\lambda \Delta\lambda + k_\phi \Delta\phi)}.$$

The stability of the scheme for a single wave number is then considered, i.e. for one $\tilde{b}_{k_\lambda, k_\phi}$.

The Fourier filter is applied directly to the tendency $\beta_{i,j}^n$, producing a filtered tendency $\hat{\beta}_{i,j}^n$ that is then used to update the divergence as

$$D_{i,j}^{n+1} = D_{i,j}^n + \Delta t \hat{\beta}_{i,j}^n.$$

To see how $\hat{\beta}_{i,j}^n$ is computed, we consider the purely zonal Fourier decomposition of the original tendency

$$\beta_{i,j}^n = \sum_{k_\lambda} \tilde{b}_{k_\lambda, j} e^{-\imath k_\lambda \Delta\lambda}$$

The filtered tendency is then given by

$$\hat{\beta}_{i,j}^n = \sum_{k_\lambda} d_{k_\lambda,j} \tilde{b}_{k_\lambda,j} e^{-\imath k_\lambda \Delta\lambda}$$

where

$$d_{k_\lambda,j} = \min\left\{1, \frac{\cos^2\phi_j}{\cos^2\phi_c} \frac{1}{\sin^2\left(k_\lambda\Delta\lambda/2\right)}\right\} \tag{A1}$$

denotes the formulation of the Fourier damping coefficients following Fox-Rabinovitz et al. (1997) (their Eq. 9). ϕ_c is the critical latitude where the Fourier filter begins to take effect, which is dependent on the aspect ratio $\alpha = \Delta\lambda/\Delta\phi$ of the grid. In particular, CAM-FV uses the condition

$$\phi_c = \arccos\left[\min\left(0.81, \Delta\phi/\Delta\lambda\right)\right]. \tag{A2}$$

For $\alpha = 1$ as generally considered in our dynamical core simulations, the critical latitude is $\phi_c \sim 36°$, whereas for the CAM-FV default aspect ratio $\alpha \sim 1.33$ the threshold lies around $\phi_c \sim 41°$. The damping is not applied to the zero mode (which represents purely meridional motion) or the largest represented wave (smallest wave number). This restricts the filter from directly affecting purely meridional motion.

To incorporate the effect of this filter into the stability analysis, we only need to consider the meridionally Fourier-transformed term $d_{k_\lambda,j}\tilde{b}_{k_\lambda,j}$. Invoking the assumption that $\cos\phi$ does not change at the grid level, we can view $d_{k_\lambda,j}$ as constant. Using the linearity of the Fourier transform, we see that the filtered tendencies of a single wave-number are given by

$$d_{k_\lambda,j}\tilde{b}_{k_\lambda,k_\phi}. \tag{A3}$$

Hence, when including the effect of the Fourier filter into the stability analysis, we only need to multiply the tendency terms by $d_{k_\lambda,j}$. To see how this affects the stability, consider

latitudes poleward of the critical latitude ϕ_c and wave numbers that involve some zonal component (not the zeroth mode, or the largest represented zonal wave). This implies

$$\Gamma_2 = 1 - 4\,C_2\,\frac{\cos^r\phi}{\cos^2\phi_c}\left\{\alpha\cos^2\phi\,\frac{\sin^2\left(k_\phi\Delta\phi/2\right)}{\sin^2\left(k_\lambda\Delta\lambda/2\right)} + \frac{1}{\alpha}\right\} \tag{A4}$$

$$\Gamma_4 = 1 - 16\,C_4\,\frac{\cos^r\phi}{\cos^2\phi_c}\left\{\alpha\cos\phi\,\frac{\sin^2\left(k_\phi\Delta\phi/2\right)}{\sin\left(k_\lambda\Delta\lambda/2\right)} + \frac{1}{\alpha\cos\phi}\sin\left(\frac{k_\lambda\Delta\lambda}{2}\right)\right\}^2. \tag{A5}$$

These equations show that the Fourier filter removes any instability present in the second-order divergence damping so long as $r \geq 0$. However, even with application of the polar filter to the fourth order divergence damping, the purely zonal wave-numbers have an amplification factor that scales as $\cos^{r-2}\phi$ which can be controlled near the poles only for $r \geq 2$ which corresponds to the default value chosen for CAM5.0.

REFERENCES

Anderson, J., T. Hoar, K. Raeder, H. Liu, N. Collins, R. Torn, and A. Avellano, 2009: The data assimilation research testbed: a community facility. *Bull. Amer. Meteor. Soc.*, **90 (9)**, 1283–1296.

Andrews, D. G. and M. E. McIntyre, 1978: An exact theory of nonlinear waves on a Lagrangian-mean flow. *J. Fluid Mech.*, **89 (4)**, 609–646.

Arakawa, A. and V. R. Lamb, 1977: Computational design of the basic dynamical process of the UCLA general circulation model. *Methods in Computational Physics*, J. Chang, Ed., Academic Press, 173–265.

Bala, G., R. Rood, D. Bader, A. Mirin, D. Ivanova, and C. Drui, 2008: Simulated climate near steep topography: Sensitivity to numerical methods for atmospheric transport. *Geo. Res. Let.*, **35**, 5 pp.

Bates, J. R., S. Moorthi, and R. W. Higgins, 1993: A global multilevel atmospheric model using a vector semi-Lagrangian finite difference scheme. Part I: Adiabatic formulation. *Mon. Wea. Rev.*, **121**, 244–263.

Boville, B. A., 1991: Sensitivity of simulated climate to model resolution. *J. Climate*, **4**, 469–485.

Colella, P. and P. R. Woodward, 1984: The piecewise parabolic method (PPM) for gas-dynamical simulations. *J. Comput. Phys.*, **54**, 174–201.

Collins, W. D., et al., 2004: Description of the NCAR Community Atmosphere Model
(CAM3.0). NCAR Tech. Note NCAR/TN-464+STR, National Center for Atmospheric
Research, Boulder, Colorado. 226 pp.

Delworth, T., et al., 2006: Gfdl's cm2 global coupled climate models. part i: Formulation
and simulation characteristics. *Journal of Climate*, **19 (5)**, 643–674.

Dey, C., 1978: Noise suppression in a primitive equation prediction model. *Mon. Wea. Rev.*,
106, 159–173.

Durran, D. R., 1999: *Numerical Methods for Wave Equations in Geophysical Fluid Dynamics.* Springer, ISBN 0-387-98376-7, 465 pp.

Fox-Rabinovitz, M. S., G. L. Stenchikov, M. J. Suarez, and L. L. Takacs, 1997: A finite-
difference GCM dynamical core with a variable-resolution stretched grid. *Mon. Wea. Rev.*,
125, 2943–2968.

Haltiner, G. J. and R. T. Williams, 1980: *Numerical Prediction and Dynamic Meteorology.*
John Wiley & Sons, ISBN 0-471-05971-4, 477 pp.

Jablonowski, C., P. H. Lauritzen, R. D. Nair, and M. A. Taylor, 2008a: Idealized test cases
for the dynamical cores of Atmospheric General Circulation Models: A proposal for the
NCAR ASP 2008 summer colloquium. Tech. rep., 74 pp. in preparation for GMD, available
online at http://www-personal.umich.edu/~cjablono/cv.html#Publication.

Jablonowski, C., P. H. Lauritzen, M. A. Taylor, and R. D. Nair, 2008b: An intercomparison
of 10 atmospheric model dynamical cores. *Eos Trans. AGU*, **89 (53)**, Abstract A33A–
0214, Fall Meet. Suppl.

Jablonowski, C. and D. L. Williamson, 2006a: A baroclinic instabilitiy test case for atmospheric model dynamical cores. *Quart. J. Roy. Meteor. Soc.*, **132 (621)**, 2943–2975.

Jablonowski, C. and D. L. Williamson, 2006b: A baroclinic wave test case for dynamical cores of General Circulation Models: Model intercomparisons. NCAR Tech. Note NCAR/TN-469+STR, National Center for Atmospheric Research, Boulder, Colorado. 89 pp.

Jablonowski, C. and D. L. Williamson, 2011: Numerical methods for global atmospheric models. *The Pros and Cons of Diffusion, Filters and Fixers in Atmospheric General Circulation Models*, P. H. Lauritzen, C. Jablonowski, M. A. Taylor, and R. D. Nair, Eds., Springer, Lecture Notes in Science and Engineering, Vol. 80, 389–504.

Lander, J. and B. J. Hoskins, 1997: Believable scales and parameterizations in a spectral transform model. *Mon. Wea. Rev.*, **125**, 292–303.

Lauritzen, P. H., 2007: A stability analysis of finite-volume advection schemes permitting long time steps. *Mon. Wea. Rev.*, **135 (7)**, 2658–2673.

Lauritzen, P. H., A. A. Mirin, J. Truesdale, K. Raeder, J. L. Anderson, J. Bacmeister, and R. B. Neale, 2011: Implementation of new diffusion/filtering operators in the CAM-FV dynamical core. *International Journal of High Performance Computing Applications*, in review.

Lin, S.-J., 2004: A "vertically Lagrangian" finite-volume dynamical core for global models. *Mon. Wea. Rev.*, **132**, 2293–2307.

Lin, S.-J. and R. B. Rood, 1996: Multidimensional flux-form semi-Lagrangian transport scheme. *Mon. Wea. Rev.*, **124**, 2046–2070.

Lin, S.-J. and R. B. Rood, 1997: An explicit flux-form semi-Lagrangian shallow water model on the sphere. *Quart. J. Roy. Meteor. Soc.*, **123**, 2477–2498.

Lindborg, E., 1999: Can the atmospheric kinetic energy spectrum be explained by two-dimensional turbulence? *J. Fluid Mech.*, **388**, 259–288.

Nastrom, G. D. and K. S. Gage, 1985: A climatology of atmospheric wavenumber spectra of wind and temperature observed by commercial aircraft. *J. Atmos. Sci.*, **42**, 950 960.

Neale, R. B., et al., 2010: Description of the NCAR Community Atmosphere Model (CAM 5.0). NCAR Technical Note NCAR/TN-XXX+STR, National Center for Atmospheric Research, Boulder, Colorado. Draft, available from http://www.cesm.ucar.edu/models/cesm1.0/cam/.

Putman, W. M. and S.-J. Lin, 2009: A finite-volume dynamical core on the cubed-sphere grid. *Numerical Modeling of Space Plasma Flows: Astronum-2008*, Astronomical Society of the Pacific Conference Series, Vol. 406, 268–276.

Rienecker, M. M., et al., 2008: The GEOS-5 data assimilation system – Documentation of versions 5.0.1 and 5.1.0. Technical Report Series on Global Modeling and Data Assimilation NASA/TM-2007-104606, NASA Goddard Space Flight Center. Pp. 92, online documentation at http://gmao.gsfc.nasa.gov/systems/geos5/.

Rood, R. B., 1987: Numerical advection algorithms and their role in atmospheric transport and chemistry models. *Rev. Geophys.*, **25**.

Sadourny, R., 1975: The dynamics of finite-difference models of the shallow-water equations. *J. Atmos. Sci.*, **32**, 680–689.

Shepherd, T. G., K. Semeniuk, and J. N. Koshyk, 1996: Sponge layer feedbacks in middle-atmosphere models. *J. Geophys. Res.*, **101**, 23 447–23 464, doi:10.1029/96JD01994.

Skamarock, W. C., 2004: Evaluating mesoscale NWP models using kinetic energy spectra. *Mon. Wea. Rev.*, **132**, 3019–3032.

Skamarock, W. C., 2008: A linear analysis of the NCAR CCSM finite-volume dynamical core. *Mon. Wea. Rev.*, **136 (6)**, 2112–2119.

Takahashi, Y. O., K. Hamilton, and W. Ohfuchi, 2006: Explicit global simulation of the mesoscale spectrum of atmospheric motions. *Geophys. Res. Lett.*, **33**, L12 812.

Williamson, D. L., J. G. Olson, and C. Jablonowski, 2009: Two dynamical core formulation flaws exposed by a baroclinic instability test case. *Mon. Wea. Rev.*, **137**, 790–796.

List of Figures

5   Vertical pressure velocity (in Pa/s) after 4 hours and 45 minutes at the CAM-FV model level near 867 hPa in the baroclinic wave test case. This shows the development of the $(2\Delta\lambda, 2\Delta\phi)$ instability of the fourth-order divergence damping when $C_4 = 0.031$. The resolution is $1° \times 1°$ with 26 vertical levels.   46

6   Amplification factor for the fourth-order damping Γ_4 with $r = 2$ (a,c) at the equator and (b,d) at $\phi = \pi/3 = 60°$. Top row (a,b): CAM 5 default configurations with $C_4 = 0.01$ and $\alpha = 1.33$. Bottom row (c,d): extreme case for $C_4 = 1/32$ and $\alpha = 1$. The axes are labeled as described for Fig. 2. Note the difference in scale.   47

7   Vertical pressure velocity (in Pa/s) at day 4 at the CAM-FV model level near 867 hPa in the baroclinic wave test. The vertical velocity is closely related to the divergence, and at the model levels is not interpolated, so the meridional waves are most apparent. Left: The default fourth-order damping $r = 2$ employs $C_4 = 0.01$, the default second-order $r = 0$ uses $C_2 = 1/128$. Right: the 2X dampings use $C_4 = 0.02$ and $C_2 = 1/64$. The resolution is $1° \times 1°$ with 26 vertical levels.   48

8   Scale-selective nature of the second and fourth-order divergence damping with $k_\lambda\Delta\lambda = k_\phi\Delta\phi$ along the x-axis. Top row (a,b): default CAM 5 with aspect ratio $\alpha = 1.33$ for Γ_2 ($r = 0$) with $C_2 = 1/128$ and Γ_4 ($r = 2$) with $C_4 = 0.01$. Bottom row (c,d): extreme cases using $\alpha = 1$ for Γ_2 ($r = 1$) with $C_2 = 1/4$ and Γ_4 ($r = 2$) with $C_4 = 1/32$. (a,c) are at the equator, (b,d) are at the latitude of $\phi = \pi/3 = 60°$.   49
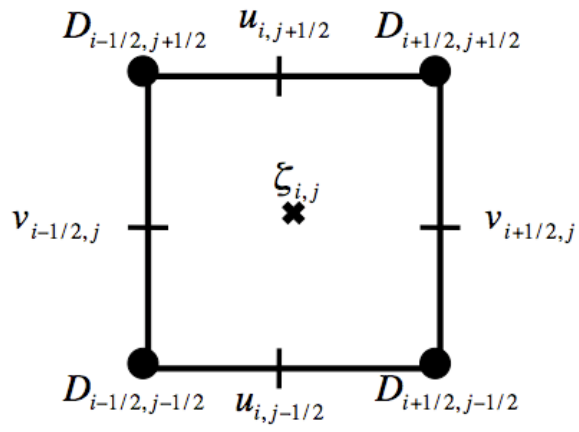
FIG. 1. Discretization of the prognostic winds (u, v) and corresponding divergence D as well as the vorticity ζ.
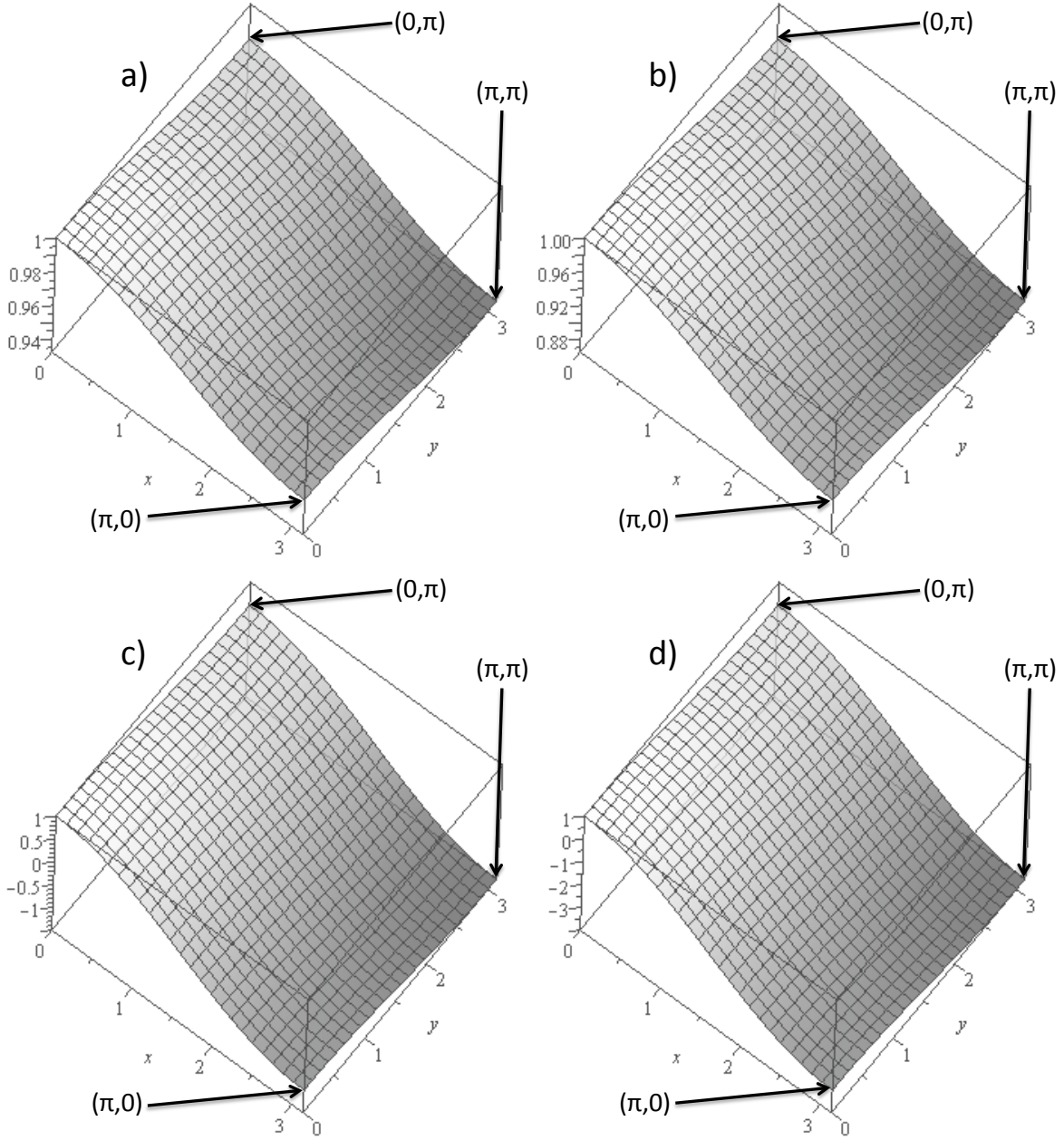
FIG. 2. Amplification factor for the second-order damping (a,c) Γ_2 for $r = 1$ and (b,d) Γ_2 with $r = 0$. The top row (a,b) shows the CAM 5 default configurations with $C_2 = 1/128$ and $\alpha = 1.33$, the bottom row (c,d) shows the extreme case with $C_2 = 1/4$ and $\alpha = 1$. All four plots are created at a latitude of $\phi = \pi/3 = 60°$. The axis labels are $x = k_\lambda \Delta\lambda$ and $y = k_\phi \Delta\phi$. Thus $x = \pi$ corresponds to the smallest resolvable wavelength of $2\Delta\lambda$. Note the differences in scale.
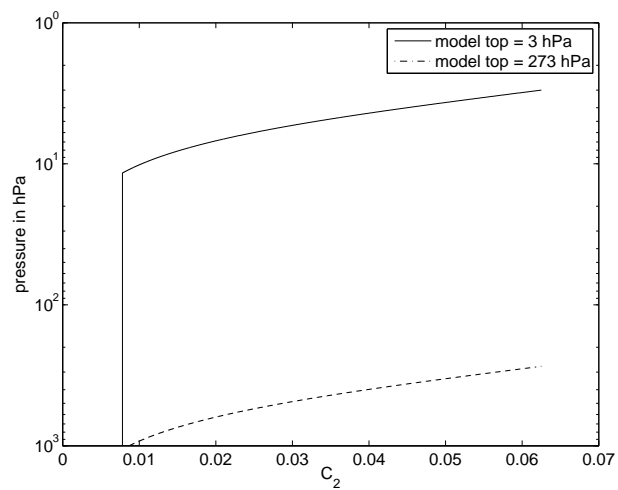
FIG. 3. Vertical profiles of the pressure-dependent multiplicative factor in the unitless parameter C_2 (Eq. 13) for a configuration with the model top at $p_{top} = 3$ hPa and $p_{top} = 273$ hPa.
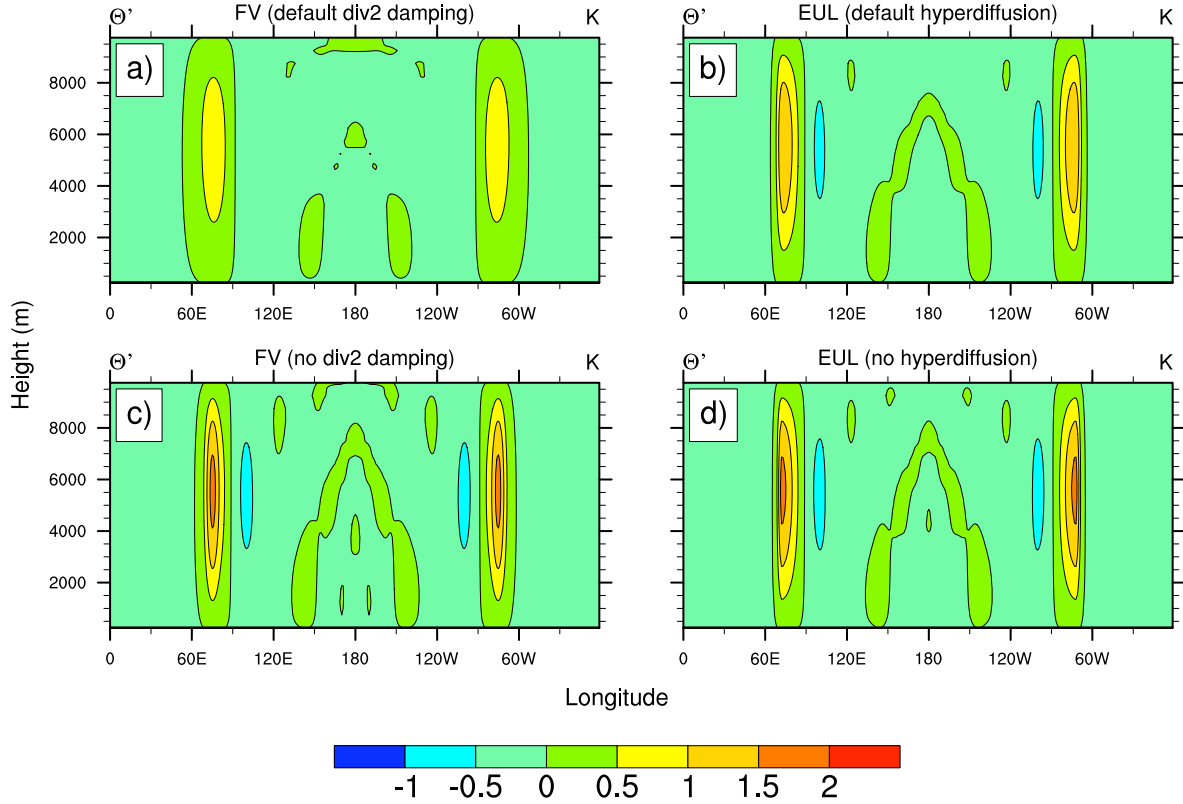
FIG. 4. Latitude-height cross section of the potential temperature perturbation (in K) at the equator in the gravity wave test case after 96 hours. (a) CAM-FV with default second-order divergence damping (vertical dependence follows the dotted line in Fig. 3), (b) CAM-EUL (spectral transform Eulerian dynamical core) including a default fourth-order hyper-diffusion term and second-order sponge layer diffusion, (c) CAM-FV without divergence damping, (d) CAM-EUL without diffusion. The resolutions are (a,c) $1° \times 1°$ and (b,d) T85 with 20 levels and a model top at 273 hPa.
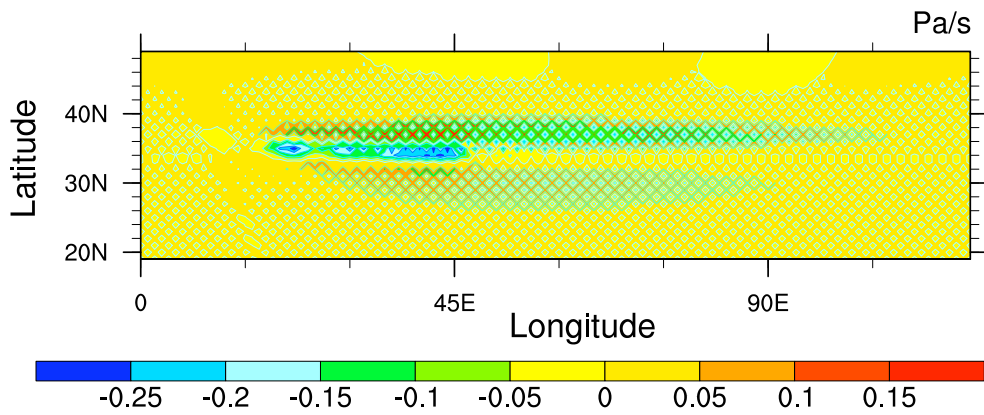
FIG. 5. Vertical pressure velocity (in Pa/s) after 4 hours and 45 minutes at the CAM-FV model level near 867 hPa in the baroclinic wave test case. This shows the development of the $(2\Delta\lambda, 2\Delta\phi)$ instability of the fourth-order divergence damping when $C_4 = 0.031$. The resolution is $1° \times 1°$ with 26 vertical levels.
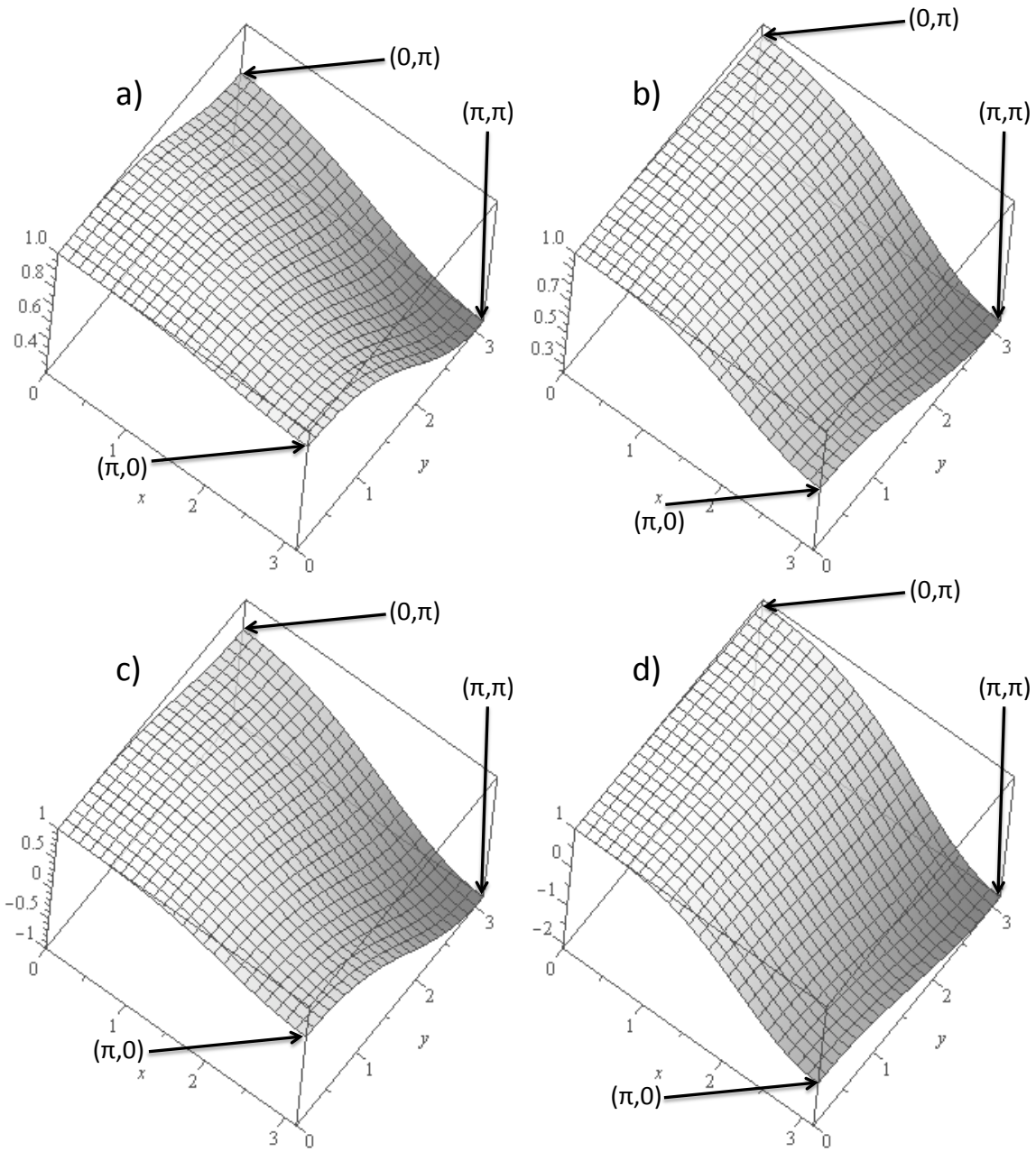
FIG. 6. Amplification factor for the fourth-order damping Γ_4 with $r = 2$ (a,c) at the equator and (b,d) at $\phi = \pi/3 = 60°$. Top row (a,b): CAM 5 default configurations with $C_4 = 0.01$ and $\alpha = 1.33$. Bottom row (c,d): extreme case for $C_4 = 1/32$ and $\alpha = 1$. The axes are labeled as described for Fig. 2. Note the difference in scale.
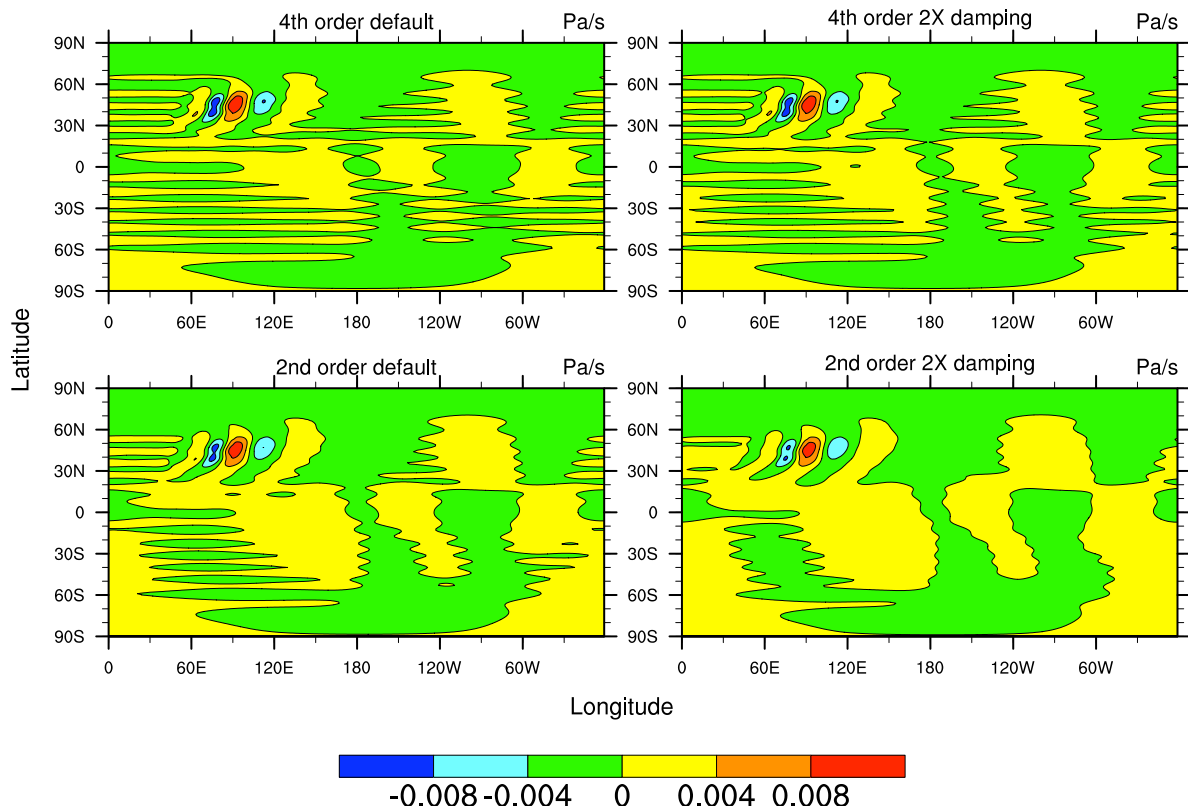
FIG. 7. Vertical pressure velocity (in Pa/s) at day 4 at the CAM-FV model level near 867 hPa in the baroclinic wave test. The vertical velocity is closely related to the divergence, and at the model levels is not interpolated, so the meridional waves are most apparent. Left: The default fourth-order damping $r = 2$ employs $C_4 = 0.01$, the default second-order $r = 0$ uses $C_2 = 1/128$. Right: the 2X dampings use $C_4 = 0.02$ and $C_2 = 1/64$. The resolution is $1° \times 1°$ with 26 vertical levels.
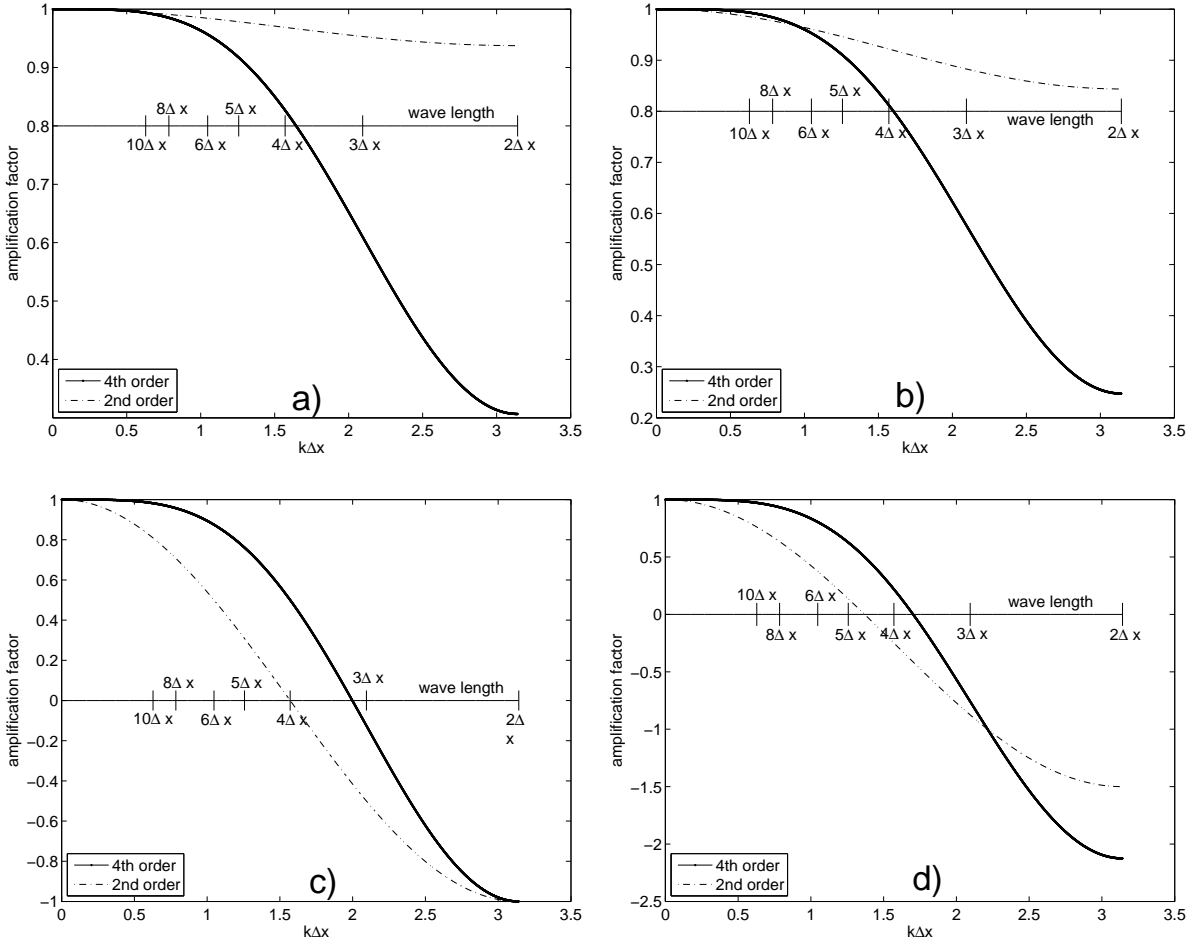
FIG. 8. Scale-selective nature of the second and fourth-order divergence damping with $k_\lambda \Delta\lambda = k_\phi \Delta\phi$ along the x-axis. Top row (a,b): default CAM 5 with aspect ratio $\alpha = 1.33$ for Γ_2 ($r = 0$) with $C_2 = 1/128$ and Γ_4 ($r = 2$) with $C_4 = 0.01$. Bottom row (c,d): extreme cases using $\alpha = 1$ for Γ_2 ($r = 1$) with $C_2 = 1/4$ and Γ_4 ($r = 2$) with $C_4 = 1/32$. (a,c) are at the equator, (b,d) are at the latitude of $\phi = \pi/3 = 60°$.